

GAMMA-RAY BLAZARS NEAR EQUIPARTITION AND THE LOCATION OF THE GAMMA-RAY EMISSION SITE IN 3C 279

CHARLES D. DERMER¹, MATTEO CERRUTI^{2,3}, BENOIT LOTT⁴, CATHERINE BOISSON³, ANDREAS ZECH³

Draft version April 25, 2013

ABSTRACT

Blazar spectral models generally have numerous unconstrained parameters, leading to ambiguous values for physical properties like Doppler factor δ_D or fluid magnetic field B' . To help remedy this problem, a few modifications of the standard leptonic blazar jet scenario are considered. First, a log-parabola function for the electron distribution is used. Second, analytic expressions relating energy loss and kinematics to blazar luminosity and variability, written in terms of equipartition parameters, imply δ_D , B' , and the principal electron Lorentz factor γ'_p . The external radiation field in a blazar is approximated by Ly α radiation from the broad line region (BLR) and ≈ 0.1 eV infrared radiation from a dusty torus. When used to model 3C 279 SEDs from 2008 and 2009 reported by Hayashida et al. (2012), we derive $\delta_D \sim 20 - 30$, $B' \sim \text{few G}$, and total (IR + BLR) external radiation field energy densities $u \sim 10^{-2} - 10^{-3}$ erg cm⁻³, implying an origin of the γ -ray emission site in 3C 279 at the outer edges of the BLR. This is consistent with the γ -ray emission site being located at a distance $R \lesssim \Gamma^2 c t_{var} \sim 0.1(\Gamma/30)^2(t_{var}/10^4 \text{ s})$ pc from the black hole powering 3C 279's jets, where t_{var} is the variability time scale of the radiation in the source frame. For low hadronic content, absolute jet powers of $\approx 10\%$ of the Eddington luminosity are calculated.

Subject headings: Gamma rays: general – Galaxies: jets – radiation mechanisms: nonthermal

1. INTRODUCTION

The time-varying emission spectrum of a blazar encodes important information about particle acceleration and radiation, jet structure and environment, and the mechanisms by which black holes power jets. Determining the jet physics and environment from the spectral energy distributions (SEDs) of blazars is a tricky problem of inversion. Part of the problem is that observational limitations make it difficult to obtain a detailed picture of the blazar SED, as the blazar continuum extends over some 20 orders of magnitude, from MHz radio frequencies to TeV γ -ray energies, and therefore requires coordinated campaigns at many wavelengths. The observing program furthermore has to be as nearly simultaneous as possible, due to the highly variable nature of blazars. In spite of these obstacles, extraordinary progress has been made to obtain a relatively complete description of the blazar SED.

The EGRET instrument on the *Compton Gamma Ray Observatory* first showed that 100 MeV – GeV emission often dominates the apparent power output of blazars during flaring states of flat spectrum radio quasars (FSRQs), and that the γ rays form a spectral component that is distinct from the nonthermal synchrotron emission radiated at radio, IR and optical frequencies

(see, e.g., Hartman et al. 1992; Wehrle et al. 1998). The ground-based Cherenkov γ -ray telescopes demonstrated that the BL Lac class are powerful sources of TeV emission (Punch et al. 1992), and that some FSRQs—3C 279 (MAGIC Collaboration 2008), PKS 1510-089 (Wagner et al. 2010; Cortina 2012), and 4C +21.35 (Aleksić et al. 2011)—are even detected at very-high energies (VHE; $\gtrsim 100$ GeV).

The Large Area Telescope (LAT) on *Fermi*, which nominally operates in scanning mode, has revolutionized our understanding of blazars by providing uninterrupted light curves and detailed SEDs of blazars. In campaigns involving radio, IR, optical, X-ray, and ground-based γ -ray telescopes, superbly detailed SEDs have been measured that challenge our theoretical understanding. A few examples include the high-synchrotron-peaked BL Lacs Mrk 421 (Abdo et al. 2011b) and Mrk 501 (Abdo et al. 2011c), the intermediate synchrotron-peaked BL Lac 3C 66A (Abdo et al. 2011d), and the FSRQs 3C 454.3 (Abdo et al. 2009) and 3C 279 (Abdo et al. 2010a). Mrk 421 and Mrk 501 are reasonably well fit with a leptonic synchrotron/SSC model, whereas an additional Compton-scattering component is required in FSRQs and low- and intermediate synchrotron-peaked BL Lac objects.

A standard blazar paradigm consisting of a magnetized plasma ejected with relativistic speeds in a collimated outflow along the polar axes of a rotating black hole has been developed to explain the overall observational features of blazars (see Boettcher et al. 2012, for a recent detailed review). But even the simple synchrotron/SSC model suffers from a proliferation of parameters, which greatly increases with the introduction of external radiation fields having uncertain spectrum and energy density. The range of possible fits to the SEDs makes it difficult to extract unique

¹ Code 7653, Space Science Division, U.S. Naval Research Laboratory, Washington, DC 20375, USA. e-mail: charles.dermer@nrl.navy.mil

² Harvard-Smithsonian Center for Astrophysics; 60 Garden Street, 02138 Cambridge, MA, USA. email: matteo.cerruti@cfa.harvard.edu

³ Laboratoire Univers et Théories (LUTH), Observatoire de Paris-Meudon, 5 Place Jules Janssen 92195 Meudon Cedex, France.

⁴ Centre d'Études Nucléaires Bordeaux Gradignan, Université de Bordeaux, CNRS/IN2P3, UMR 5797, Gradignan, 33175, France

and therefore meaningful blazar jet properties. Part of this difficulty has to do with characterizing the non-thermal electron spectrum, and another part with the range of possibilities of external photon sources, which can include the accretion-disk (Dermer et al. 1992; Dermer & Schlickeiser 1993; Dermer & Schlickeiser 2002), broad line region (BLR; Sikora et al. 1994), and molecular torus (Błażejowski et al. 2000; Arbeiter et al. 2002; Sokolov & Marscher 2005) radiations (see also Böttcher 2007; Sikora et al. 2009).

To help alleviate these problems, we adopt a specific model where the target radiation fields are the BLR radiation and IR radiation from a dusty torus surrounding the nucleus. We employ a log-parabola function in Section 2 to describe the electron energy distribution in the comoving fluid frame. Equipartition relations between the energy densities of the magnetic field, the nonthermal electrons, and the observed properties of the blazar synchrotron spectrum are derived in Section 3. In Section 4, model results are shown for target photons of the external radiation described by monochromatic frequencies and various energy densities. Spectral fitting of recent SEDs of 3C 279 (Hayashida et al. 2012) are used to illustrate the method.

In a companion paper (Cerruti et al. 2013), we improve the model for the external radiation field, replacing monochromatic infrared emission by thermal spectra, and the BLR radiation field by a complex of atomic emission lines rather than by the Ly α line alone. We show that scattering of the BLR radiation under equipartition conditions can explain the GeV spectral cutoff discovered with *Fermi*-LAT in 3C 454.3 and other FSRQs and low- and intermediate-synchrotron-peaked BL Lac objects (Abdo et al. 2009, 2010b).

2. LOG-PARABOLA ELECTRON DISTRIBUTION

In leptonic blazar jet models, the synchrotron and Compton γ -ray emission components are radiated by nonthermal electron distributions that are assumed to be isotropic in the jet fluid frame. One technique is to fit the data by injecting power-law particle distributions and allowing the particles to evolve in response to radiative and adiabatic energy losses (e.g., Böttcher & Chiang 2002; Moderski et al. 2003). This approach requires many parameters for the cutoff energies, injection indices, and power, but is potentially useful to follow dynamic blazar spectral behavior.

Contrary to this approach, we abandon any preconceptions about particle acceleration, and employ the simplest functional form that is able to provide reasonably good fits to the snapshot SED data.⁵ For this purpose, we assume that the log-parabola function

$$\log[\gamma'^2 N'_e(\gamma')] = \log[\gamma_p'^2 N_e(\gamma_p')] - b \log(\gamma'/\gamma_p')^2 \quad (1)$$

gives a good description of the nonthermal electron Lorentz-factor (γ') distribution $N'_e(\gamma')$ in the comoving fluid frame, where the electron distribution is assumed to be isotropic. The entire description of the electron energy distribution is then given by three parameters: the normalization, the peak (or principal) Lorentz factor γ'_p , and the spectral curvature parameter b . Electrons with

$\gamma' \approx \gamma'_p$ therefore contain the maximum nonthermal electron energy per unit logarithmic interval $\Delta(\log \gamma')$ in the electron distribution. Thus

$$\gamma'^2 N'_e(\gamma') = \gamma_p'^2 N'_e(\gamma_p') \left(\frac{\gamma'}{\gamma_p'}\right)^{-b \log(\frac{\gamma'}{\gamma_p'})}, \quad (2)$$

that is, the electron distribution function is a smoothly curving function with continuously varying spectral index. Normalizing to the total comoving nonthermal electron energy \mathcal{E}'_e through $\mathcal{E}'_e = m_e c^2 \int_1^\infty d\gamma' \gamma' N'_e(\gamma')$ gives $\mathcal{E}'_e \cong m_e c^2 \gamma_p'^2 N'_e(\gamma_p') I(b)$, where $I(b) = \sqrt{\pi \ln 10}/b$ ($\sqrt{\pi \ln 10} \simeq 2.69$). Note that the relationship is not exact, because we have replaced $1/\gamma_p'$ with 0 in the lower limit of the integral.

The log-parabola function has been used to describe blazar (Massaro et al. 2004) and gamma-ray burst (Massaro et al. 2010) spectra. It has also been recognized as a convenient functional form for the electron energy distribution (Massaro et al. 2006), and is treated in detail by Tramacere et al. (2011).

3. EQUIPARTITION RELATIONS

One goal is to determine, by comparison with blazar SED data, whether the synchrotron and γ -ray spectra are reasonably well fit by a log-parabola function for the electron energy distribution, within the scenario that the blazar jet is described by a standard relativistic jet model with quasi-isotropic electrons trapped in a randomly oriented magnetic field with mean strength B' in the fluid frame. The principal comoving electron Lorentz factor γ'_p functions like the minimum Lorentz factor in a fast-cooling blast-wave scenario (Sari et al. 1998), but here only represents instantaneous or time-averaged (not evolving) particle and photon distributions.

3.1. Parameters and Derived Quantities

In the stationary frame of the black-hole/jet system, we can list the important observables that describe the blazar SED:

1. $L_s = 10^{48} L_{48} \text{ erg s}^{-1}$, the apparent isotropic bolometric synchrotron luminosity;
2. $\epsilon_s = h\nu_s/m_e c^2 = 8.13 \times 10^{-7} \nu_{14}$, the peak synchrotron frequency, that is, the frequency at which the $\nu_L \nu$ synchrotron spectrum reaches its maximum value, in units of $m_e c^2$, where $10^{14} \nu_{14} \text{ Hz}$ is the peak synchrotron frequency in the source frame;
3. $t_{var} = 10^4 t_4 \text{ s}$, the variability time scale, where $t_{var} = t_v^{obs}/(1+z)$, and t_v^{obs} is the measured variability time scale;
4. $A_{EC} \equiv L_{EC}/L_s$, the external Compton-dominance factor giving the ratio of the apparent isotropic γ -ray luminosity, assumed to be from Compton scattering of external isotropic radiation, to L_s ; and
5. $A_{SSC} \equiv L_{SSC}/L_s$, the internal, or self-Compton-dominance factor, giving the ratio of the SSC luminosity to L_s . This ratio is more difficult to determine from the blazar SED, because the SSC component is concealed by the EC component, though it may be reveal at hard X-ray energies.

⁵ Finke et al. (2008) uses a similar approach for SSC modeling of TeV blazars.

A complete SED contains additional information in the detailed features of the spectrum.

Within the framework we set up, the derived synchrotron/SSC/EC model parameters are:

1. B' , the comoving magnetic field, in G;
2. δ_D , the Doppler factor;
3. γ'_p , the principal electron Lorentz factor;
4. $r'_b = c\delta_D t_{var}$, the comoving radius of the emission region;
5. u_0 , the external radiation field energy density; and
6. $\epsilon_0 = h\nu_0/m_e c^2$, the dimensionless external radiation photon frequency.

The dynamical crossing time associated with the Schwarzschild radius of a $10^9 M_\odot$ black hole is $\approx 10^4$ s. For only a few extremely bright blazar flares does the *Fermi* LAT have sensitivity to probe to a few hour time scale (Abdo et al. 2011a; Tanaka et al. 2011; Foschini et al. 2011), and detection of much more rapid variability from TeV blazars (e.g., Aharonian et al. 2007; Aleksić et al. 2011) represents a major puzzle. To keep the exposition uncluttered (but incomplete), we let $t_4 = 1$ in our calculations, keeping in mind that this parameter should be determined by observations of the variability properties of the blazar at the time that the observing campaign took place.

The comoving magnetic field energy density $u'_{B'} = B'^2/8\pi$. In the standard blazar model, we can normalize the total energy density u'_{tot} of particles, field, and radiation in the outflowing plasma blob through the expression

$$u'_{tot} = u'_{B'}(1 + \zeta_{par} + \zeta_{ph}) = u'_{B'}(1 + \zeta_e + \zeta_{p/nuc} + \zeta_s + \zeta_*) . \quad (3)$$

The subscripts here refer to magnetic field (B'), including both large-scale and turbulence and MHD waves; particles (par), divided into nuclear (p/nuc) and electronic (e) components; and photons (ph), consisting of the internal synchrotron (s) and external (*) radiation-field energy densities in the comoving frame. In the Thomson regime, $A_{SSC} = L_{SSC}/L_s = u'_s/u'_{B'} \approx \zeta_s$, and $A_{EC} = L_{EC}/L_s = u'_*/u'_{B'} \approx \zeta_*$.

The simplest equipartition relation is $u'_e = \zeta_e u'_{B'}$, $\zeta_e \cong 1$, which also minimizes jet power. We let $\zeta_{p/nuc} = 1$ in the following calculations, which is the upper limit to a jet with low baryon content. The baryonic content affects only the total power and not spectral properties; see Section 6.4.

3.2. Constraints and Equipartition Relations

One advantage of using the log-parabola function, besides having only three parameters to characterize the nonthermal electron distribution, is that in the limit $b \rightarrow \infty$, the electrons become monoenergetic. Here we solve in that limit, and use the analytic results to provide parameters as input for a numerical model.

A first constraint arises from simple kinematics. In a blob geometry, the comoving synchrotron energy density $u'_s = L_s^{kin}/4\pi r_b'^2 c\delta_D^4$, where $r'_b = c\delta_D t_{var}$, so

$$L_s^{kin} = 4\pi r_b'^2 c\delta_D^4 u'_s . \quad (4)$$

A second constraint, which is exact in the limit $b \rightarrow \infty$, is the synchrotron luminosity constraint

$$L_s^{syn} = \frac{4}{3} c\sigma_T u'_{B'} N_0 \gamma_p'^2 \delta_D^4 . \quad (5)$$

When the equipartition relation $m_e c^2 N_0 \gamma_p'/V'_b = u'_e = \zeta_e u'_{B'}$, with $V'_b = 4\pi r_b'^3/3$, is substituted into the synchrotron constraint, eq. (5), and the result is equated with the luminosity given by the kinematic constraint, eq. (4), we find

$$\zeta_s = \frac{4}{9} \sigma_T u'_{B'} \frac{r_b'}{m_e c^2} \zeta_e \gamma_p' . \quad (6)$$

In the $b \rightarrow \infty$ asymptote, the peak synchrotron frequency can be expressed in terms of the critical magnetic field $B_{cr} = m_e^2 c^3 / e\hbar$ as

$$\epsilon_s = \frac{3}{2} \frac{B'}{B_{cr}} \gamma_p'^2 \delta_D , \quad (7)$$

from which, with eq. (6), we derive

$$\delta_D B'^3 = \frac{3}{2 B_{cr} \epsilon_s} \left(\frac{18\pi m_e c \zeta_s}{\sigma_T t_{var} \zeta_e} \right)^2 . \quad (8)$$

Replacing this result in eq. (4) gives

$$\begin{aligned} \delta_D &= \left(\frac{2L_s^3}{3^{10} \pi^4 \zeta_s^7 c^{13}} \right)^{1/16} \left(\frac{\sigma_T \zeta_e}{m_e} \right)^{1/4} \left(\frac{B_{cr} \epsilon_s}{t_{var}} \right)^{1/8} \\ &\cong 17.5 L_{48}^{3/16} \frac{\zeta_e^{1/4} \nu_{14}^{1/8}}{\zeta_s^{7/16} t_4^{1/8}} . \end{aligned} \quad (9)$$

Inverting eq. (7) to get an expression for B' as a function of δ_D , and using eq. (9) for δ_D gives

$$B'(\text{G}) \cong \frac{5.0 \zeta_s^{13/16}}{L_{48}^{1/16} t_4^{5/8} \nu_{14}^{3/8} \zeta_e^{3/4}} . \quad (10)$$

Using eqs. (7), (9), and (10), we have

$$\gamma_p' \cong 523 \frac{\nu_{14}^{5/8} \zeta_e^{1/4}}{L_{48}^{1/16} \zeta_s^{3/16} t_4^{3/8}} . \quad (11)$$

3.3. EC Component

In the Thomson regime, the peak frequency of the external Compton-scattered component is

$$\epsilon_C^{EC} = \frac{4}{3} (\delta_D \gamma_p')^2 \epsilon_* \cong 2.2 \times 10^3 \frac{\zeta_e}{\zeta_s^{5/4}} \nu_{14}^{3/2} L_{48}^{1/4} \sqrt{t_4} \epsilon_{Ly\alpha} . \quad (12)$$

The onset of the Klein-Nishina correction for external Compton scattering takes place when $4\gamma_p' \epsilon' \gtrsim 1$. Taking $\epsilon' \cong \delta_D \epsilon_*$, the photon energy in the stationary frame where KN effects become important is at $\epsilon_{C,KN} = 1/12 \epsilon_*$. For Ly α photons with $\epsilon_* = 2 \times 10^{-5}$, $E_{C,KN} \cong 2.2$ GeV, and this could be the reason for the spectral cut-off in FSRQs and LSP blazars (Ackermann et al. 2010; Cerruti et al. 2013).

3.4. SSC Component

The peak SSC Compton γ -ray frequency is approximately given by

$$\begin{aligned} \epsilon_C^{SSC} &\cong \frac{4}{3} \delta_D \gamma_p'^2 \epsilon_s' \cong \frac{4}{3} \gamma_p'^2 \epsilon_s \\ &\cong \frac{9.4 \times 10^3}{L_{48}^{1/8}} \frac{\zeta_e^{1/2}}{\zeta_s^{3/8}} \left(\frac{\nu}{10^{16} \text{Hz}} \right)^{9/4} t_4^{3/4}. \end{aligned} \quad (13)$$

The onset of Klein-Nishina effects in SSC scattering takes place at photon energy $\epsilon_s \gtrsim \epsilon_{s,\text{KN}} = \delta_D/4\gamma_p'$, implying

$$\epsilon_{s,\text{KN}} \cong 8.4 \times 10^{-3} \frac{L_{48}^{1/4}}{\zeta_s^{1/4} \sqrt{t_4 \nu_{14}}}, \quad (14)$$

or

$$\nu_{14,\text{KN}} \cong 474 \frac{L_{48}^{1/6}}{\zeta_s^{1/6} t_4^{1/3}}. \quad (15)$$

Thus, KN effects are most important in high-synchrotron peaked (HSP; $\nu_s^{\text{obs}} > 10^{15}$ Hz) BL Lac objects.

3.5. Synchrotron Self-Absorption

We use the δ -function approximation to calculate synchrotron self-absorption (SSA). The SSA coefficient for a photon of frequency $m_e c^2 \epsilon'/h$ in the fluid frame is given in this approximation by

$$\kappa_{\epsilon'} = \frac{-\pi}{36} \frac{\lambda_C r_e}{\epsilon'} \left[\gamma_s' \frac{\partial}{\partial \gamma_s'} \left(\frac{n_e'(\gamma_s')}{\gamma_s'^2} \right) \right], \quad \gamma_s' = \sqrt{\epsilon'/2\epsilon_B'}, \quad (16)$$

(Dermer & Menon 2009, eq. (7.144), with corrections). Here $\lambda_C = h/m_e c$ is the Compton wavelength, $r_e = e^2/m_e c^2$ is the classical electron radius, and $\epsilon_B' = B'/B_{cr}$. Taking $n_e'(\gamma') = N_e'(\gamma')/V_b'$, and substituting Equation (2) for $N_e'(\gamma')$ gives

$$\kappa_{\epsilon'} = \frac{\pi}{18} \frac{\mathcal{E}_e'}{m_e c^2 I(b) V_b' \gamma_p'^4} \frac{\lambda_C r_e}{\epsilon'} (2 + b \log x) x^{-(4+b \log x)}, \quad (17)$$

where $x \equiv \sqrt{\epsilon'/2\epsilon_B'}/\gamma_p'$.

The SSA opacity $\tau_{\epsilon'} = 2\kappa_{\epsilon'} r_b'$. The unabsorbed spectrum is multiplied by the factor $u(\tau) = 1/2 + \exp(-\tau)/\tau - [1 - \exp(-\tau)]/\tau^2$, with $\tau = \tau_{\epsilon'}$, to give the absorbed spectrum.

3.6. Jet Power

We calculate absolute jet power L_{jet} using the relation

$$L_{jet} = 2\pi r_b'^2 \beta \Gamma^2 c u'_{tot}, \quad (18)$$

for a two-sided jet (Celotti & Fabian 1993; Celotti & Ghisellini 2008), where the total internal energy density u'_{tot} is given by Equation (3). This equation is surely valid for isotropic particles and randomly oriented fields, but the photon distributions in the comoving frame have peculiar isotropies not taken into account by Equation (18), which make the different angular distributions of synchrotron and Compton radiation fluxes (Dermer 1995).

For photon powers, we therefore use expressions relating apparent isotropic and absolute photon fluxes

(Dermer et al. 2012, Appendix A). The apparent ($L_{iso,s}$) and absolute ($L_{abs,s}$) synchrotron fluxes are related by the expression

$$L_{abs,s} = 8\Gamma^2 L_{iso,s} / 3\delta_D^4, \quad (19)$$

and a similar expression likewise holds for the SSC fluxes. For external Compton (C) fluxes, the relationship is

$$L_{abs,C} = 32\Gamma^4 L_{iso,C} / 5\delta_D^6, \quad (20)$$

and

$$L_{ph} = L_{abs,s} + L_{abs,C}. \quad (21)$$

These very different behaviors are important for power requirements in photon-dominated jets. The kinetic power $2\Gamma \mathcal{E}'/t_{var}$ required by the jet to transport the radiating electrons and magnetic field is found to be much smaller than the photon power, so that baryon-loading does not have a big impact on jet power requirements until it is $\gtrsim 10\times$ the electron energy.

4. NUMERICAL RESULTS

Using the derived values of δ_D , B' , γ_p' , and r_b' , along with the log-parabola description of the electron spectrum, Equation (1), we numerically calculate νL_ν SEDs. The methods for calculating the SEDs are presented in Finke et al. (2008) and Dermer et al. (2009). We use the head-on approximation for Compton scattering (Jones 1968), which is valid for relativistic electrons ($\gamma \gg 1$) scattering lower-energy photons ($\epsilon \ll \gamma$), with Klein-Nishina effects fully taken into account (Dermer & Menon 2009).

In the model calculations shown in this section, we calculate SEDs for external isotropic photon sources with $\epsilon_* = 2 \times 10^{-5}$ characterizing the BLR (10.2 eV), and $\epsilon_* = 2 \times 10^{-7}$ (0.1 eV) describing radiation from the dust torus. The former value is motivated by the strong Ly α line in blazars, specifically, 3C 454.3 (Bonnoli et al. 2011), and the latter value by calculations of AGN emissions reprocessed by a dust clouds Nenkova et al. (2008,?). The peak power of the reprocessed emission occurs at $\approx 10\mu$ (the 10μ silicate feature), with broad wings from $\approx 3\mu$ to $\approx 30\mu$. This peak frequency correspond to $\epsilon_* \approx 2 \times 10^{-7}$, or an effective blackbody temperature of ≈ 440 K, characteristic of warm dust.

Relevant for characterizing the IR environment of blazars are recent observations of the unusual FSRQ 4C +21.35 by. Malmrose et al. (2011). They analyzed 5 – 35 μ Spitzer, Sloan Digital Sky Survey, Two Micron All Sky Survey, and Swift UVOT data of 4C +21.35, decomposing its spectrum into a nonthermal power law and two-temperature dust model, made of a warm dust component with effective temperature $T \sim 660$ K radiating $\approx 10^{45}$ erg s $^{-1}$, and a hot dust component with $T \approx 1200$ K radiating $\approx 8 \times 10^{45}$ erg s $^{-1}$, both on the pc scale. We examine hot dust fits for 3C 279 below, but consider warm dust ($\epsilon_* = 2 \times 10^{-7}$) for an initial parameter study.

When fitting actual blazar spectra, both IR dust and BLR photon sources contribute and have to be appropriately adjusted to give a good fit. Detailed fitting requires a range of atomic lines and multiple thermal components (Cerruti et al. 2013), but this two-line simplification illustrates this approach to modeling the SEDs of blazars

TABLE 1
OBSERVATIONAL BLAZAR INPUT^a

<i>i</i>	L_{48}	ϵ_*	ν_{14}	t_4	b	ζ_s	ζ_*	N_Γ
1a	1	2×10^{-5}	0.1	1	1	0.5	10	1
1b								0
1c		2×10^{-7}						
1d								1
2a	0.1	2×10^{-5}	0.1	1	1	0.5	10	1
2b								0
2c		2×10^{-7}						
2d								1
3a1	0.01	2×10^{-5}	0.1	1	1	0.5	10	1
3a2		2×10^{-7}						
3b1		2×10^{-5}	1					
3b2		2×10^{-7}						
3c1		2×10^{-5}	10					
3c2		2×10^{-7}						
4a ^b	0.001	—	1	1	1	0.5	—	1
4b			10^1					
4c			10^2					
4d			10^3					
4e			10^4					

^a $\zeta_e = \zeta_{ep} = 1$; blank entries in Tables are equal to first vertical entry above.

^b Equipartition synchrotron/SSC model

TABLE 2
BLAZAR MODEL OUTPUT

<i>i</i>	Γ	δ_D	B' (G)	γ'_p	u_0 (erg cm ⁻³)	r'_b (10 ¹⁵ cm)	$\log[L_{jet}(L_{ph})]$ (erg s ⁻¹)
1a	17.8	17.8	6.75	141.2	0.0431	5.33	46.6(47.1)
1b	8.89				0.172		46.0(46.5)
1c							46.0(46.8)
1d	17.8				0.0431		46.6(47.4)
2a	11.5	11.5	7.80	163.	0.136	3.46	46.0(46.5)
2b	5.77				0.545		45.4(45.9)
2c							45.4(46.1)
2d	11.5				0.136		46.6(47.1)
3a	7.49	7.49	9.00	1.88e2	0.431	2.25	45.4(46.1)
3b	9.99	9.99	3.80	7.94e2	0.0431	3.00	45.1(45.9)
3c	13.3	13.3	1.60	3.35e3	0.00431	4.00	44.9(45.4)
4a	6.49	6.49	4.38	9.17e2	—	1.95	43.9(44.4)
4b	8.65	8.65	1.85	3.97e3		2.59	43.7(44.0)
4c	11.5	11.5	0.78	1.63e4		3.46	45.4(43.6)
4d	15.4	15.4	0.33	6.88e4		4.61	43.2(43.3)
4e	20.5	20.5	0.14	2.90e5		6.15	42.9(43.0)

in order to derive basic properties of the jet and environment.

Figure 1 shows the resulting model SEDs for values characteristic of a very powerful FSRQ blazar with a

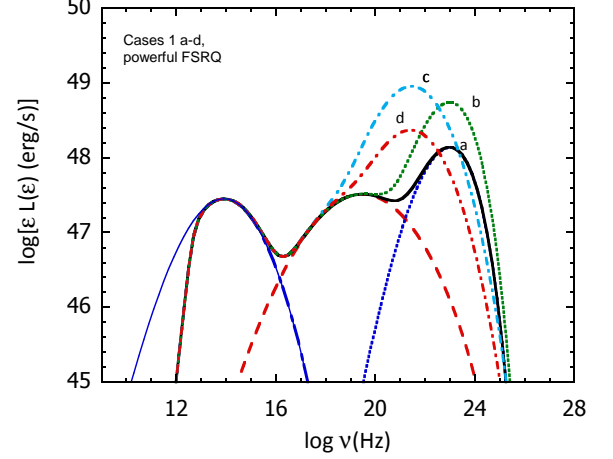


FIG. 1.— Model blazar SEDs from the radio to the γ -ray implied by near-equipartition conditions, using synchrotron luminosities and peak frequencies characteristic of a powerful FSRQ like 3C 454.3. In this calculation, $\zeta_s = 0.5$ and $\zeta_* = 10$. The bolometric apparent synchrotron luminosity $L_s = 10^{48}$ erg s⁻¹. The jets are viewed off axis ($\theta \cong 1/\Gamma$ in a and d, and on-axis in b and c). The target photons are Ly α ($\epsilon_* = 2 \times 10^{-5}$) in a and b, and IR dust photons ($\epsilon_* = 2 \times 10^{-7}$) in c and d. Separate synchrotron, SSC, and EC components are shown for a. Thin solid line shows the synchrotron emission component in the absence of self-absorption.

bolometric synchrotron luminosity $L_s = 10^{48}$ erg s⁻¹ and peak photon frequency $\nu_s = 10^{13}$ Hz. Input values for this and subsequent figures in this section are given in Table 1, and derived values are listed in Table 2. In the calculations, we use the relation

$$\Gamma = \frac{1}{2} (1 + N_\Gamma^2) \delta_D \quad (22)$$

to relate Γ and δ_D , where $N_\Gamma = \Gamma\theta$, valid in the limit $\Gamma \gg 1$, $\theta \ll 1$. We consider two cases: $N_\Gamma = 1$, cases 1a and 1d, and $N_\Gamma = 0$, cases 1b and 1c. We also use a single external monochromatic line appropriate to the BLR ($\epsilon_* = 10.2/511000$) in cases a and b and an IR torus ($\epsilon_* = 2 \times 10^{-7}$) in cases c and d.

Already we see an interesting result: a break at GeV energies is formed when jet electrons scatter Ly α /BLR photons, but not when scattering IR photons, which instead make νF_ν peaks near 10 MeV. If the electrons in the flaring jet are within the BLR, they scatter both IR and BLR photons, whereas when the radiating jet is found far outside the BLR, scattering of IR photons dominates. So an FSRQ with a GeV break would also be accompanied by a γ -ray external Compton dust feature. In contrast, flares occurring far outside the BLR would make a blazar SED peaked at MeV energies, as seen in some low-frequency peaked blazars, e.g., CTA 102 and PKS 0528+134, as indicated by joint OSSE, COMPTEL, and EGRET analysis (McNaron-Brown et al. 1995).

The different beaming factors of the synchrotron and SSC components on the one hand and the EC components on the other are seen when the νL_ν SED for $\theta = 1/\Gamma$, $\delta_D = \Gamma$ is compared with the SED for $\theta = 0$, $\delta_D = 2\Gamma$ (Dermer 1995; Georganopoulos et al. 2001). In Figure 1, $\Gamma \approx 18$ for $\theta = 1/\Gamma$ and $\Gamma \approx 9$ for $\theta = 0$, with photon energy densities $u_0 \approx 0.043$ erg cm⁻³ and $u_0 = 0.17$ erg cm⁻³ corresponding to SSC and EC factors $\zeta_s = 0.5$ and $\zeta_* = 10$, respectively. A larger energy density is required

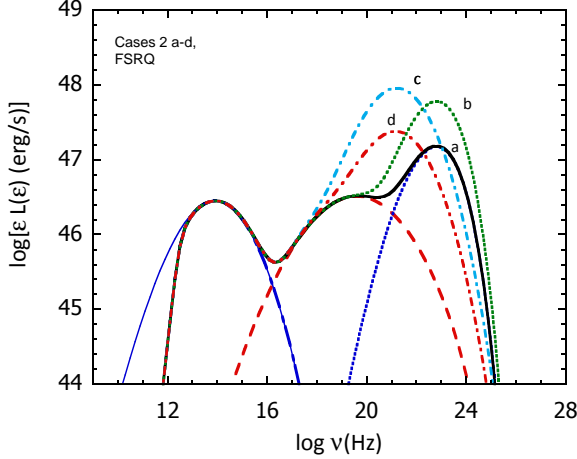


FIG. 2.— Same as for Fig. 1, except that $L_{\text{syn}} = 10^{47} \text{ erg s}^{-1}$, characteristic of powerful blazars like 3C 279.

for the on-axis jet model, because the implied Γ factor is smaller.

Even though $\zeta_s = 0.5$ in Figure 1, the SSC luminosity is about equal to the synchrotron luminosity. This is because the log-parabola function is not a simple δ -function, and the electrons with $\gamma' > \gamma'_p$ are more effective scatterers than lower energy electrons, insofar as the Thomson energy-loss rate $|\dot{\gamma}_T| \propto \gamma'^2$. This also accounts for shifting of the model peak frequency to $\nu_s > 10^{13} \text{ Hz}$. In the limit that $b \rightarrow \infty$, $\nu_s = 10^{13} \text{ Hz}$. For the same reason, the peak frequency of the Compton-scattered dust component gets shifted to higher energies than expected from simple Thomson estimates. When $\theta \approx 1/\Gamma$, the Thomson-scattered γ -ray luminosity L_γ of the dust component is about $\zeta_*(=10) \times$ larger than L_s , but is even larger when viewed down the jet axis due to the different beaming factors. The Compton-scattered Ly α component has a smaller apparent luminosity than that of the dust component because of the onset of Klein-Nishina effects. The absolute jet luminosities for these cases almost reach the Eddington luminosity for a $10^9 M_\odot$ black hole when $\theta = 1/\Gamma$, but are significantly less for the on-axis viewing.

Figure 2 shows a calculation similar to Figure 1, but with an order-of-magnitude smaller apparent bolometric synchrotron luminosity, now with $L_s = 10^{47} \text{ erg s}^{-1}$. The values of Γ become smaller than in the cases shown in Figure 1, but the energy densities of the external radiation fields must become larger in order to produce the same Compton dominance (see Table 2). The absolute jet powers become smaller, though not as fast as decreasing $\propto L_s^{-1}$. Again, the equipartition solution ($\zeta_e = 1$) with $t_4 = 1$ gives a breaking GeV spectrum from target Ly α photons, while the upscattered IR photons peak at $\sim 1 - 10 \text{ MeV}$ in a νF_ν SED, while breaking at slightly higher energies. IR radiation from hot dust would increase the break energy by a factor ~ 3 , still well below the GeV range.

Figure 3 shows calculations for parameters characteristic of Intermediate Synchrotron Peaked (ISP) blazars, defined (Abdo et al. 2010c) as blazars with observed peak synchrotron frequencies in the range $10^{14} \text{ Hz} < \nu_s^{\text{obs}} < 10^{15} \text{ Hz}$. The synchrotron and external Comp-

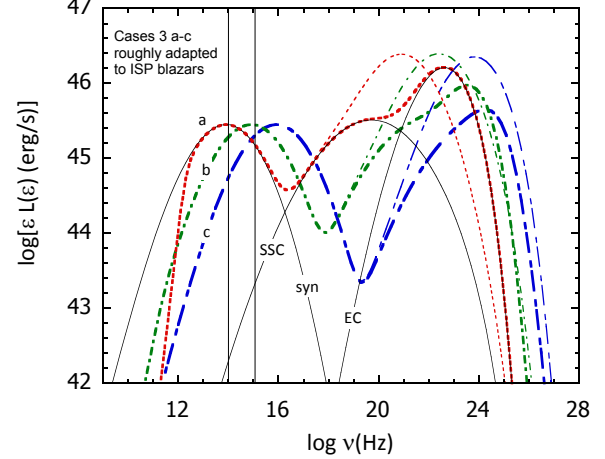


FIG. 3.— Near-equipartition models with input parameters characteristic of ISP blazars like 3C 66A and W Comae. Here $L_{\text{syn}} = 10^{46} \text{ erg s}^{-1}$, $\zeta_s = 0.5$ and $\zeta_* = 10$, and a range of values of $\nu_s = 0.1, 1$, and 10 are chosen. Vertical lines show the range bounding peak synchrotron frequencies ν_s defining ISP blazars, defined by $10^{14} \text{ Hz} < \nu_s < 10^{15} \text{ Hz}$, defined according to Abdo et al. (2010c). Thick lines are for Ly α photons, and thin lines are for 1200 K IR photons from the dusty torus. Separate components, including the unabsorbed synchrotron emission, are shown for case a with target Ly α photons.

ton parameters are kept as before, with $\zeta_s = 0.5$ and $\zeta_* = 10$, but the value of ν_{14} is allowed to vary from 0.1 to 10 . The different SEDs for target IR and Ly α radiation fields are shown by the thin and thick curves, respectively. Notice that values of ν_s that give $10^{14} \text{ Hz} \lesssim \nu_s \lesssim 10^{15} \text{ Hz}$ are really about an order of magnitude smaller for $b = 1$, as explained above. The discrepancy decreases with increasing b , and becomes exact in the limit $b \rightarrow \infty$.

Depending on the source redshift, the cases shown in Figure 3 could all qualify as ISP blazars. The increase in ν_s coincides with an increase in Γ , but with a reduction of u_0 because of the increased efficacy of Compton scattering an external isotropic radiation field when Γ is larger. The onset of Klein-Nishina effects reduces the importance of the Compton-scattered Ly α field, so that the SED is dominated by γ rays produced from target IR torus photons. In one of the cases shown, the peak and cutoff from scattered IR photons is near 1 GeV . If in fact, the dust torus was the dominant target photon source for the blazar γ -ray SED, then a linear correlation between the γ -ray and synchrotron peak frequencies is predicted.

For these ISP-type parameters, structure may be found in the GeV regime due to the competition between SSC and Compton-scattered Ly α photons. There is also the possibility of an inverted spectrum when the EIC emission starts to dominate the SSC emission. Such a feature may be present in the SED of 3C 66A (Abdo et al. 2011d), but will require better data and fitting to establish.

Figure 4 shows equipartition models for blazars with characteristics similar to those of HSP BL Lac objects. Comparison of the SEDs of Mrk 421 and Mrk 501 from multiwavelength campaigns of Abdo et al. (2011b) and Abdo et al. (2011c), respectively, with models 4c and 4d suggest that these TeV BL Lac objects will be well fit

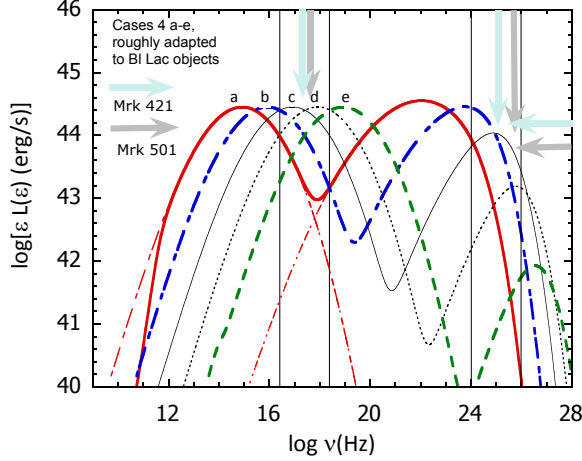


FIG. 4.— Near-equipartition SSC models characteristic of nearby BL Lac objects like Mrk 421 and Mrk 501. The model shows results for $L_{syn} = 10^{45}$ erg s $^{-1}$, $\zeta_s = 0.5$, and $\log \nu_{14} = 1, 2, 3, 4, 5$, corresponding to curves a through e, respectively. Vertical lines define the range of average peak synchrotron and Compton frequencies for Mrk 421 and Mrk 501, and light and dark arrows point to values of ν_s , $\nu_{L\nu_s}$, ν_C , and $\nu_{L\nu_C}$ for Mrk 421 and the Mrk 501, respectively, from the campaigns reported in Abdo et al. (2011b) and Abdo et al. (2011c).

with our equipartition model. The broader widths of the synchrotron and Compton SED components in Mrk 501 compared to Mrk 421 resulting from a smaller b in the log-parabola description of the electron energy distribution can help explain the differences in ν_C and $\nu_{L\nu_C}$ between these two sources.

For this parameter set, we also calculated the energy density of Ly α radiation needed to make a significant contribution to the γ -ray fluxes. When $u_{Ly\alpha} \gtrsim 10^{-4}$ erg cm $^{-4}$, the emission would make an EC component with $\nu_{L\nu_C} \gtrsim 10^{41.5}$ erg s $^{-1}$, just barely visible in the $\nu_{L\nu}$ spectrum. The Ly α energy densities in Mrk 421 and Mrk 501 are, however, far below this level. Stocke et al. (2011) report Ly α luminosities of 2.4 and 5.2×10^{40} erg s $^{-1}$ for Mrk 421 and Mrk 501, respectively. The total jet power is $\approx 10^{44}$ erg s $^{-1}$ for the models in Fig. 4, and the accretion-disk luminosity L_d should be greater than this if most of the jet energy comes from mass accretion (black-hole rotational energy could supply a comparable amount). Even for a BLR as small as 0.01 pc, the Ly α energy density $u_{Ly\alpha} \approx 10^{40} L_{40} / 4\pi R_{0.01pc}^2 c \approx 3 \times 10^{-5}$ erg cm $^{-3}$, far smaller than what is necessary to make the EC γ -ray flux brighter than the SSC flux.

The low Ly α luminosities of Mrk 421, Mrk 501, and also PKS 2005-489 and PKS 2155-304 (Stocke et al. 2011), two other HSP BL Lac objects, validates the presumption that TeV blazars have a very tenuous BLR environment. By contrast, FSRQs can have very large Ly α luminosities; in the case of 3C 454.3 (Bonnoli et al. 2011), reaching $\approx (2-4) \times 10^{45}$ erg s $^{-1}$.

A complete model SED requires, for consistency, the emission spectrum from the accretion-disk and from the dust. The accretion-disk spectral luminosity is assumed to be described by a Shakura-Sunyaev spectrum given by

$$\epsilon L_{disk}(\epsilon) = 1.12 L_{disk} \left(\frac{\epsilon}{\epsilon_{max}} \right)^{4/3} \exp(-\epsilon/\epsilon_{max}), \quad (23)$$

TABLE 3
BLAZAR INPUT PARAMETERS FOR 3C 279^a

Epoch	L_{48}	ν_{14}	ϵ_{IR}	ζ_s	$\zeta_{Ly\alpha}$	ζ_{IR}	L_{disk} (10^{46} erg s $^{-1}$)
A	0.06	0.01	2×10^{-7}	0.06	8	4	0.55
A ^b			5.4×10^{-7}		6	12	
B	0.15	0.02	2×10^{-7}	0.04	14	11	1.0
B ^b	0.1	0.05	5.4×10^{-7}	0.1	18	8	0.5
C ^c	0.18	0.02	2×10^{-7}	0.04	7	2.2	0.2
D ^{c,d}	0.18	0.03		0.045	16	5	0.5

^a $t_4 = \zeta_e = \zeta_{p/nuc} = N_\Gamma = b = 1$; $\epsilon_{BLR} = 2 \times 10^{-5}$

^bHot dust solutions: $T = 1200$ K, $\epsilon_{IR} = 5.4 \times 10^{-7}$

^cNo hot dust solutions with $t_4 = \zeta_e = 1$

^dIn this fit, $b = 1.1$

normalized such that $\int_0^\infty d\epsilon L(\epsilon) = L_{disk}$, so that $\Gamma(4/3) \cong 1/1.12$. The νF_ν spectrum of the accretion-disk is therefore $f_{\epsilon_{obs}}^{ad} = \epsilon L_{disk}(\epsilon) / 4\pi d_L^2$, where $\epsilon = (1+z)\epsilon_{obs}$ and d_L is the luminosity distance. The value of ϵ_{max} depends on the spin of the black hole and relative Eddington luminosity, but for simplicity we let $\epsilon_{max} = 10$ eV, typical of the characteristic temperature of the UV bump in Seyfert galaxies.

The spectral luminosity of the IR dust component is approximated by a thermal distribution normalized to the IR luminosity L_{IR} . Thus

$$\epsilon L_{IR}(\epsilon) = \frac{15 L_{IR}}{\pi^4} \frac{(\epsilon/\Theta)^4}{\exp(\epsilon/\Theta) - 1}, \quad (24)$$

with corresponding νF_ν spectrum $f_{\epsilon_{obs}}^{IR} = \epsilon L_{IR}(\epsilon) / 4\pi d_L^2$. Here $\Theta = k_B T / m_e c^2 = 2 \times 10^{-7}$, taking $T = 1200$ K. A dust covering factor of 20% is assumed, so that $L_{IR} = 0.2 L_{disk}$. The energy density of the IR radiation is limited by the energy density of a blackbody, namely

$$u_{bb}(\text{erg cm}^{-3})(T) = 9.36 \times 10^{24} \Theta^4 \\ \cong 3 \times 10^{-4} \left(\frac{T}{440 \text{ K}} \right)^4 \cong 0.016 \left(\frac{T}{1200 \text{ K}} \right)^4 \quad (25)$$

Thus the energy density at most reaches $\approx 10^{-3}$ erg cm $^{-3}$ for warm dust, and ≈ 0.02 erg cm $^{-3}$ for hot dust.

5. MODELING THE SEDS OF 3C 279

Hayashida et al. (2012) have organized 3C 279 campaigns around Fermi-LAT with wonderful results. The data in Figures 5 and 6 show SEDs from quasi-simultaneous observing campaigns for four periods of Fermi-LAT observation, namely Epochs A (MJD 54682 - 54729; 4 Aug 2008 - 19 Sept 2008), B (MJD 54789 - 54809; 19 Nov 2008 - 9 Dec 2008), C (MJD 54827 - 54877; 27 Dec 2008 - 15 Feb 2009), and D (MJD 54880 - 54885; 18 Feb 2009 - 23 Feb 2009). The SEDs comprise X-ray data from Suzaku,⁶ Swift XRT, XMM Newton and RXTE, optical/UV data from Kanata, GROND and Swift UVOT (170-650 nm), IR data from Spitzer, and radio data from CARMA and OVRO. These SEDs are contemporaneous and not strictly simultaneous, as different telescopes require different observing intervals to achieve the displayed sensitivity. Nevertheless, these

⁶ *Suzaku* consists of the XIS (0.3-12 keV), HXD/PIN (10-700 keV), and HXD/GSO (40-600 keV).

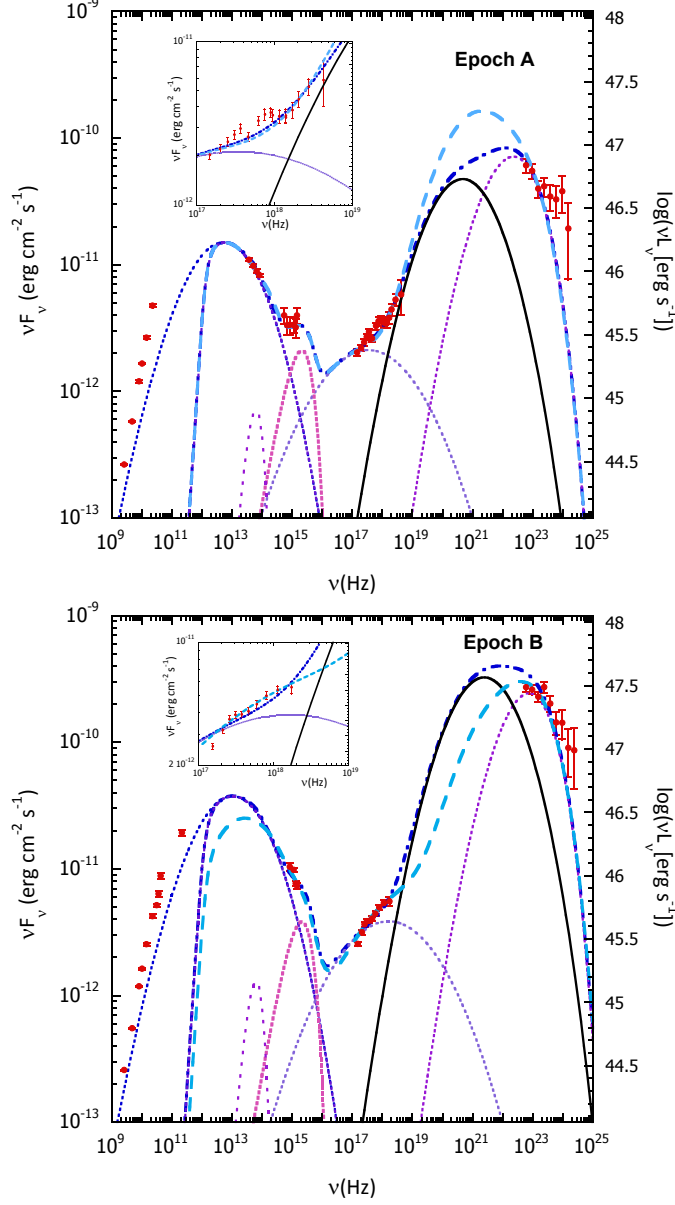


FIG. 5.— Near-equipartition blazar model fits (by eye) to the SEDs of 3C 279 (Hayashida et al. 2012) for Epochs A (upper panel) and B (lower panel), with input parameters given in Table 3 and implied quantities from the model in Table 4. Dot-dashed curves and components, peaking from low to high-frequencies, are the optically thin and absorbed nonthermal synchrotron emission, the thermal dust emission, the accretion-disk radiation, and SSC, EC dust, and EC Ly α emission components assuming a warm dust target with $\epsilon_{IR} = 2 \times 10^{-7}$. Dashed curves show modeling with hot dust, $\epsilon_{IR} = 5.4 \times 10^{-7}$. Insets show detail of fits at X-ray energies.

SEDs are some of the most detailed FSRQ spectra yet measured.

Figures 5 and 6 also show by-eye fits to 3C 279 from our equipartition model. This approach is restricted to sources with known redshift, and the redshift of 3C 279 is particularly well known ($z = 0.5362$; Marziani et al. 1996). Putting in observables t_{var} , L_{syn} and $\nu_{pk,syn}$ gives δ_D , B' and r'_b through the equipartition formulation, Equations (9), (10), and (11), respectively. With

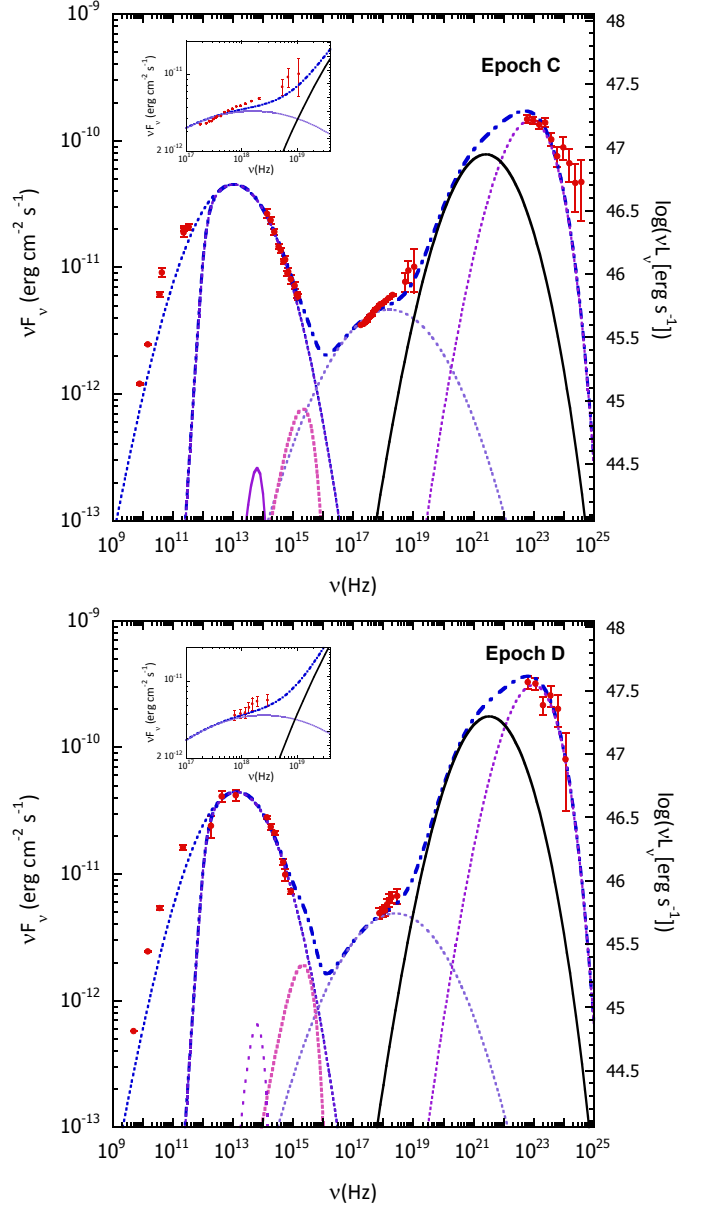


FIG. 6.— Near-equipartition blazar model fits to the SEDs of 3C 279 (Hayashida et al. 2012) for Epochs C (upper) and D (lower), with input parameters given in Table 3 and derived quantities in Table 4. Components as in Fig. 5.

the goal of limiting the number of parameters, we take $t_4 = \zeta_e = \zeta_{p/nuc} = N_\Gamma = b = 1$, and vary only L_{48} , ν_{14} , ζ_s , ζ_{EC} and ζ_{dust} ($\zeta_{EC} + \zeta_{dust} = \zeta_*$). In fact, t_{var} can be measured, as can N_Γ if the angle to the jet axis can be determined, and such values should be used when available. The value $\zeta_{p/nuc}$ only affects the jet power, not the spectrum, as is proved by examining Equations (3), (18), and (9) – (11). Relaxing ζ_e away from unity, which increases the jet power, can be used as a last resort, but for the purposes of the study of a system in electron/magnetic field equipartition, we keep $\zeta_e = 1$.

In the fitting, there is some freedom to assign the accretion-disk temperature and luminosity, and therefore dust luminosity for the assumed 20% covering factor.

TABLE 4
MODEL OUTPUT VALUES FOR 3C 279

Epoch	Γ, δ_D	B' (G)	γ'_p	$u_{Ly\alpha}$ (10^{-3} erg cm^{-3})	u_{IR} (10^{-3} erg cm^{-3})/ $T_{min}(\text{K})^a$	$\log[L_{jet}(L_{ph})]$ (erg s $^{-1}$)
A	20.7	3.2	60.4	5.6	2.8/776	46.3(46.0)
A ^b				4.2	8.5/1024	46.4(46.2)
B	30.8	1.8	93.4	1.4	1.1/610	46.7(46.3)
B ^b	21.4	2.7	143	8.8	3.9/840	46.5(46.4)
C ^c	31.8	1.8	92.3	0.64	0.22/410	46.4(45.9)
D ^c	31.8	1.7	116	1.3	0.41/480	46.7(46.2)

^aMinimum blackbody temperature to exceed u_{IR}

^bHot dust solutions

^cNo hot dust solutions with $t_4 = \zeta_e = 1$

Sometimes the accretion-disk emission is important to fit structure in the optical, but in other cases gives only an upper limit to disk luminosity L_{disk} .

The results of fitting, by eye, the data for Epochs A-D of 3C 279 are shown in Figures 5 and 6 and listed in Tables 3 and 4. The spectral components and total spectra are shown in these figures for the case of a warm dust IR field ($\epsilon_{IR} = 2 \times 10^{-7}$). The different components, as written in the figure caption, are the unabsorbed and synchrotron self-absorbed nonthermal synchrotron spectra, the IR graybody field, the Shakura-Sunyaev accretion-disk field (big blue bump), the SSC, EC γ rays from dust and, at the highest energies, EC from $Ly\alpha$. For comparison, we also show fits in Fig. 5 with a hot-dust external IR target radiation field ($\epsilon_{IR} = 5.4 \times 10^7$). In both these cases, we were able to find hot dust solutions, facilitated in the Epoch B case by its poorly defined synchrotron component.

We could not find solutions that gave acceptable fits to Fig. 6 for the hot dust solution, provided we keep the other parameters, in particular, t_4 and ζ_e fixed to unity. In these cases, the Compton-scattered IR component had little effect on the rising X-ray component, and the SSC radiation peaked at too low of a frequency to match the Swift XRT data. The model fits with the warm dust appear to simulate well enough the blazar spectra. In Epochs A and B, we can also obtain good fits with hot dust. In fact, the dust emission spectrum is far broader than a black body, so more detailed examination must consider scattering a broad-band IR spectrum.

6. DISCUSSION

In the *Fermi* era, the blazar SED can be detailed enough as in the case of 3C 279 (Hayashida et al. 2012) that each model component is required and constrained by the data: the nonthermal synchrotron component, of course, for the nonthermal radio/mm/IR/optical radiations; accretion-disk radiations to explain the optical/UV blue bump; nonthermal SSC X-rays; hard X-rays observed by the Swift XRT and BAT and NuStar made by SSC and Compton-scattered IR (EC-IR) photons originating from outside the jet; and GeV γ rays by external Compton scattering of $Ly\alpha$ and BLR photons (EC-BLR). If the models lacked the EC-IR γ -ray component, the model SEDs would be very different, both at the lower end of the Fermi-LAT range and in the hard X-ray/soft γ -ray spectrum explored by Swift BAT, Suzaku, INTE-

GRAL, and NuStar. Note that accretion-disk radiations are required to obtain good fits to the optical spectra in Epochs A and B, and the model does not apply to the $\lesssim 10^{12}$ Hz radio measurements.

6.1. Model Implications

In this approach to multiwavelength FSRQ modeling, fitting to a blazar SED implies values of δ_D , B' , γ'_p , and r'_b for a specific value of t_{var} and observing angle θ . Our fits to the multi-epoch data from 3C 279, Figs. 5 and 6, imply $\Gamma \approx \delta_D \approx 20 - 30$ and $B' \approx \text{few G}$, assuming $\theta = 1/\Gamma$ and $t_4 = 1$. These values are not too different from earlier determinations of these numbers in work by Błażejowski et al. (2000)⁷ and Hartman et al. (2001)⁸ when fitting to multiwavelength data associated with earlier EGRET campaigns, where reasonable fits were obtained by guessing values for Γ and B' .

Assuming that the technique implying Γ and B' give results that correspond to the actual conditions of the radiating jetted plasma expelled by the black hole, then the energy densities of the surrounding radiation fields are derived with an uncertainty reflecting the range of parameters that yield a good fit to the data. It is not, however, easy to say what that uncertainty is without a detailed numerical study. Here our aim is more limited: to demonstrate the ability of the equipartition model to extract jet and environmental parameters.

6.2. Location of γ -ray production site

Epochs A – D range in duration from 6 days (Epoch D) to 3 weeks (Epoch B) and 6 weeks (Epochs A and C), and statistics accumulated during these observing times show up in the error bars of the Fermi-LAT SEDs shown in Figs. 5 and 6 (Hayashida et al. 2012). The derived target photon energy densities for Epochs A – D of 3C 279 are $u_{Ly\alpha} \approx 10^{-2} - 10^{-3}$ erg cm $^{-3}$ for the $Ly\alpha$ field and $u_{IR} \approx 10^{-2} - 10^{-4}$ erg cm $^{-3}$ for the IR field, ranging over a factor of ~ 40 for the different fits. The total energy density of the external radiation field is $\approx 10^{-2} - 10^{-3}$ erg cm $^{-3}$. The $Ly\alpha$ radiation comprises nearly one-third of the broad line flux (Telfer et al. 2002), and the total broad line flux may amount to $\approx 10\%$ of the accretion-disk luminosity reprocessed by BLR gas.

Simple scaling relations from reverberation mapping studies indicate that the BLR radius R_{BLR} can be written in terms of the accretion-disk luminosity L_{disk} through the expression

$$R_{BLR} \cong 0.1 \sqrt{\frac{L_{disk}}{10^{46} \text{ erg s}^{-1}}} \text{ pc} . \quad (26)$$

(Ghisellini & Tavecchio 2008). If a fraction $\tau < 1$ of the radiation is scattered or reprocessed into line radiation, then Equation (26) implies that the energy density of the scattered radiation is

$$u_{scatt} \approx \frac{L_{disk}\tau}{4\pi R_{BLR}^2 c} \cong 0.03 \left(\frac{\tau}{0.1}\right) \text{ erg cm}^{-3} . \quad (27)$$

so that the typical energy density of $Ly\alpha$ radiation in the BLR is at the level of $(0.01 - 0.1)$ erg cm $^{-3}$, consistent

⁷ $B' = 0.81$ G, $\Gamma = 20$, $\theta = 1/\Gamma = 2.86^\circ$, $\gamma_{br} = 150$

⁸ $B' = 1.5$ G, $\Gamma = 5 - 15$, $\theta = 2^\circ$; observing angle from Lähteenmäki & Valtaoja (1999)

with the derived energy densities of Epoch A. At later Epochs, the inferred $\text{Ly}\alpha$ energy density is well below $\approx 0.01 \text{ erg cm}^{-3}$.

If the emission region is at the outer edges of the BLR, in this case at $\gtrsim 0.1 \text{ pc}$, then the derived $\text{Ly}\alpha$ energy densities could be consistent with all Epochs A–D, including the hot-dust solutions for Epochs A and B. Note that the IR energy densities for a characteristic temperature are constrained by Equation (25). For the derived IR energy density, we give the minimum blackbody temperature, T_{\min} , in Table 4. From the derived energy densities shown in Table 4, we see that the largest required IR energy densities for a hot dust solution is compatible with the blackbody temperature, whereas the warm dust solutions are marginally compatible with the blackbody limit. The warm dust solutions in Epochs C and D are compatible with the blackbody limits.

For the hot dust solution, the energy density of 1200 K blackbody radiation is $\approx 0.02 \text{ erg cm}^{-3}$, from Equation (25). The radius of a 1200 K blackbody radiating $10^{45} L_{45} \text{ erg s}^{-1}$ of thermal radiation is $R_{bb} \approx 0.13 \sqrt{L_{45}}$ pc. The smaller derived values of the IR dust energy density, $u_{IR} = 10^{-3} u_{-3} \text{ erg cm}^{-3}$ ($0.2 \lesssim u_{-3} \lesssim 6$), are consistent with the same luminosity, but from a larger region of characteristic size $R_{IR} \cong \sqrt{u_{bb}/u_{IR}} R_{bb} \approx 0.5/\sqrt{u_{-3}}$ pc.

The IR luminosity that we assume for 3C 279 is small by comparison with other sources. For 4C +21.35, an FSRQ like 3C 279, thermal IR radiation with a luminosity of $7.9 \pm 0.2 \times 10^{45} \text{ erg s}^{-1}$ was measured, as was a weak detection of dust from the FSRQ CTA 102 with IR luminosity of $7 \pm 2 \times 10^{45} \text{ erg s}^{-1}$ (Malmrose et al. 2011). On the other hand, an upper limit on dust emission of $2.3 \times 10^{45} \text{ erg s}^{-1}$ was found for PKS 1510–089, another FSRQ. The IR luminosity derived by fitting the 3C 279 SED (Table 3), $L_{IR} \sim 1 - 2 \times 10^{45} \text{ erg s}^{-1}$, is somewhat lower than these values, but this number could be increased by factors of several by assuming a smaller dust covering factor, without affecting the model fits. We can write $u_{dust} [\text{erg cm}^{-3}] \cong 3 \times 10^{-3} (L_{IR}/10^{45} \text{ erg/s}) / (R/10^{18} \text{ cm})^2$, with the characteristic size scale of about 1 lt-yr for the IR in 3C 279.

Energy densities of target radiation fields can vary from one epoch to another for two reasons: (i) by changing locations of the emitting jet plasma to places with different ambient radiation fields, or (ii) by having the jet γ -ray production take place at a similar location while the surrounding radiation environment changes. With a dynamical time of $\approx 1 \text{ yr}$ for the IR field, and variations in u_{IR} by $\gtrsim 10$ from the warm dust solutions over the seven months comprising the 4 Epochs studied, case (i) seems preferred. Indeed, we can use Epoch A, for which the largest value of u_{IR} , $u_{-3} \approx 6$ was derived, to argue that the characteristic size of the IR torus could be as small as $\approx 0.2 \text{ pc}$. The γ -ray emission at later Epochs could be made at $\gtrsim 0.5 \text{ pc}$ from the black hole, where the IR field is smaller, consistent with the smaller energy densities of radiations inferred in later Epochs.

6.3. Jet Model

Within the colliding shell paradigm, the collision radius $R_{coll} \lesssim 2\Gamma_a^2 ct_{var} \sim 0.2(\Gamma/30)^2 t_4 \text{ pc}$, which is also at the outer perimeter of the BLR (Eq. (26)). Collision

radii of relativistic plasma ejecta seem consistent with a location at the edge of BLR, which is also on the $\sim 0.1 - 0.5 \text{ pc}$ size scale of the IR dust emission where u_{IR} changes significantly. In Epoch A, when the derived Γ is smallest, so $R_{coll} \lesssim \Gamma_a^2 ct_{var} \sim 0.03(\Gamma/17)^2 t_4 \text{ pc}$, the probable location of the emission region is deep within the BLR and IR torus. If the IR torus is on size scales as small as 0.2 pc , which depends on dust properties, then the size scales are similar. From Nenkova et al. (2008), the inner radius due to dust sublimation is

$$R_d \simeq 0.4 \sqrt{L_{45}} \left(\frac{T_{sub}}{1500 \text{ K}} \right)^{2.6} \text{ pc}, \quad (28)$$

where the bolometric AGN luminosity is $10^{45} \text{ erg s}^{-1}$, and T_{sub} is the dust sublimation temperature. Malmrose et al. (2011) argue for dust sublimation radius of $1 - 2 \text{ pc}$. It could also be that the IR zone is not much larger than the BLR, as might follow naturally if the torus and BLR clouds are the same accretion flow found at different distances from the nuclear continuum, with properties defined by whether the accreting flow was inside or outside the dust-sublimation radius (Nenkova et al. 2008).

6.4. Jet Power

The absolute 2-sided jet power is given by Equation (18), $L_{jet} = 2\pi r_b'^2 \beta \Gamma^2 cu'_{tot}$, with $u'_{tot} = u'_{B'}(1 + \zeta_e + \zeta_{p/nuc} + \zeta_s + \zeta_*)$ for the total energy density, from Equation (3). The jet power $L_{jet} (\text{erg s}^{-1})$ is reported in Table 4 for the 4 Epochs of 3C 279. We also give the photon power $L_{ph} = L_{ph,syn} + L_{ph,EC}$, from Equations (19) and (20) for the synchrotron/SSC and EC photon powers, respectively. A value of $\zeta_{p/nuc} = 1$ is assumed in the values of L_{jet} given in Table 4. The maximum jet power found in our calculations, again with baryon-loading unity, is $L_{jet} \approx 10^{46.7} \text{ erg s}^{-1} \approx 5 \times 10^{46} \text{ erg s}^{-1}$.

This number should be compared with the Eddington luminosity. From emission line studies, Gu et al. (2001); Woo & Urry (2002) infer a black hole of mass $(3 - 8) \times 10^8 M_\odot$ in the 3C 279 system. The implied Eddington luminosities are in the range $(4 - 10) \times 10^{46} \text{ erg s}^{-1}$. It is worth remarking that if Eddington conditions limit maximum jet power, then the most powerful flare is at the Eddington limit, provided $\zeta_{p/nuc}$ is sufficiently small. The absolute jet powers for the warm-dust solutions, in units of $10^{47} \text{ erg s}^{-1}$, the maximum Eddington luminosity, are $\zeta_{p/nuc} = (1, 10, 100) = (0.14, 0.2, 0.95)$ for Epoch A, $(0.54, 0.71, 2.5)$ for Epoch B, $(0.26, 0.46, 2.4)$ for Epoch C, and $(0.46, 0.63, 2.3)$ for Epoch D. To keep the absolute jet luminosity $\lesssim 10^{47} \text{ erg s}^{-1}$ in all cases requires a baryon-loading factor $\zeta_{p/nuc} \lesssim 30$. The photon power is the dominant component of the the power budget in the jets of 3C 279; see Table 4.

The apparent isotropic bolometric γ -ray luminosity exceeds $\approx 10^{48} \text{ erg s}^{-1}$ in Epoch B, whereas the absolute jet power, dominated by photons, is $\sim 5 \times 10^{46} \text{ erg s}^{-1}$, for low hadronic content, $\zeta_{p/nuc} = 1$. Reduction of power requirements is a consequence of the jet opening angle $\theta \approx 1/\Gamma$, which leads to beaming factors $f_b \sim 0.1\%$ for $20 \lesssim \Gamma \lesssim 30$. The reduction from apparent to absolute jet power should follow the solid angle reduction according to the beaming factor $f_b = 1.7 \times 10^{-3}$ in Epoch A, and $\theta \approx 1/30 \text{ rad}$; $f_b \cong 6 \times 10^{-4}$ in later epochs. The

reduction in power is not by the full beaming factor because it depends on the beaming cone of the radiation.

6.5. Particle Acceleration and the Highest Energy γ rays

As a fitting function, the log-parabola spectrum seems to be capable of fitting multiwavelength blazar data reasonably well, even with b fixed to unity. Such curving functions are well known to arise in second-order, stochastic acceleration scenarios (e.g., Park & Petrosian 1995; Becker et al. 2006). If the quality of fits are better and if fewer parameters are used in the current framework than employed in shock/injection scenarios, we may conclude that the curving spectrum is a better model for the data.

A shock framework may still be required in a second-order acceleration scenario, because turbulence induced downstream of a shock might be required for acceleration. A turbulent scenario might also naturally arise in some version of models involving jet reconnection in compact knots far (\gtrsim pc) from the nucleus (e.g., Giannios et al. 2009), and Poynting-dominated jet models. An interesting question is why the $b = 1$ solution is a good first approximation to the electron spectrum.

With regard to the fits to 3C 279, it is clear that in Epochs A, B, and C, the model underproduces the \gg GeV emission measured by Fermi-LAT. This deficiency cannot be corrected by using a better BLR model (Cerruti et al. 2013), and the MAGIC Collaboration (2008) detection of VHE photons from 3C 279 seems to require either leptonic scenarios far out of equilibrium⁹ or hadronic processes (Böttcher et al. 2009). In view of emission extending to the VHE range, a new spectral component may be required, and the best candidate is one made by UHECRs accelerated in blazars. As we have seen, the jet powers can accommodate large baryon-load factors, $\zeta_{p/nuc} \lesssim 30$, so 3C 279 or, indeed, other powerful FSRQs, could display high-energy hadronic emission tails (Atoyan & Dermer 2003).

6.6. Hadronic Acceleration and UHECRs

From the Hillas (1984) condition, $E_{max} \cong \Gamma Z e B' r'_b \cong Z e c B' \Gamma \delta_D t_{var} \cong 1.6 \times 10^{20} Z (B'/2 \text{ G}) (\Gamma/30) (\delta_D/30) t_4 \text{ eV}$. Thus 3C 279 is not prevented from accelerating protons to super-GZK energies by this basic requirement. FSRQs like 3C 279 are, however, unlikely to be the solution to the origin of the UHECRs, insofar as no FSRQs are found within the GZK radius of $\sim 100 - 200$ Mpc. In spite of their great power, the low space density of FSRQs and powerful FR2 radio galaxies makes them unlikely to be the primary source class powering the UHECRs. For that, FR1 radio galaxies and BL Lac objects are favored (Dermer & Razzaque 2010; Murase & Takami 2009). These types of blazars have trouble, however, accelerating protons to energies $\gtrsim 10^{19}$ eV, above which the composition must become heavy (Murase et al. 2012).

UHECR production in FSRQs like 3C 279 might be revealed by cascade radiation induced by photopion pro-

duction from escaping UHECR protons. At redshift $z = 0.5362$, angular size distance $d_A = 1301.8 \text{ Mpc}$ ($H_0 = 71 \text{ km (s-Mpc)}^{-1}$, $\Omega_m = 0.27 = 1 - \Omega_\Lambda$). Depositing energy on a distance scale of $100 - 200 \text{ Mpc}$ with a jetted beam pointed nearly along our line of sight will create through photopion and photopair processes a steady, extended γ -ray emission feature (Essey & Kusenko 2010; Essey et al. 2010). Under certain conditions, the UHECR beam can escape from the structured regions surrounding the 3C 279 nucleus without dispersal (Murase 2012).

A blazar like 3C 279, in the ecliptic plane, at latitude 0.2° , is not preferentially located for IceCube observations, but otherwise would be a promising target for PeV neutrino searches. The external Ly α radiation field provides a target for ultra-relativistic protons to make a neutrino spectrum down to PeV energies (see Fig. 3 in (Dermer et al. 2012); contrary to statements of Cholis & Hooper (2012)).

6.7. Blazar Divide and Sequence

One of the most impressive blazar correlations in Fermi-LAT blazar studies is the γ -ray spectral index versus γ -ray luminosity (Abdo et al. 2010c). A particularly noticeable separation between the BL Lacs and FSRQs in this plane is referred to as the blazar divide (Ghisellini et al. 2009), and interpreted in terms of different accretion regimes, expressed as an Eddington ratio. The object 3C 279 occupies, no surprise, a position consistent with a soft-spectrum FSRQ, with $\Gamma \cong 2.31$ below the 3.5 GeV break and a steeper spectrum, $\Gamma \cong 2.95$, above (Hayashida et al. 2012).

When the blazar sequence (Fossati et al. 1998) and also blazar divide are fit by simple blazar models, one obtains a typical electron Lorentz factor $\langle \gamma \rangle$ (Ghisellini et al. 1998), and the general relation is that the peak electron Lorentz factor $\gamma'_{peak} \sim \gamma'_p \sim \langle \gamma \rangle$ is inversely correlated with L_γ , where L_γ is the average apparent isotropic γ -ray power), though the detailed behavior is unclear and in dispute (Meyer et al. 2011).

Obtaining an inverse correlation of γ'_p and L_γ is not obvious in a first-order acceleration scenario involving a wind of power $L = L_w > L_\gamma$, where maximum particle energy $\propto L^{1/2}$. In cooling scenarios, the cooling Lorentz factors go to lower energies when the radiation field is more intense (Ghisellini et al. 1998; Böttcher & Dermer 2002; Finke 2012).

In a second-order acceleration scenario, the inverse correlation of γ'_p and L_γ can be obtained if the scale of turbulence $\lambda_{max} \propto 1/k_{min}$ grows with increasing L_γ . To show this, note that the most important losses are synchrotron and Thomson, with loss rate $-\dot{\gamma}_{syn,T} = K_{syn,T} L \gamma^2$, assuming $B^2/8\pi + U_\gamma \propto L$. The energy-gain rate from gyroresonant acceleration of electrons or ions with Alfvénic turbulence is

$$\dot{\gamma}'_{acc} = \frac{\pi}{2} \left(\frac{q-1}{q} \right) c k'_{min} \beta_A'^2 \zeta(r'_L k'_{min})^{q-2} \gamma'^{q-1} \quad (29)$$

(Dermer et al. 1996), where q is the spectrum of the turbulence and $r'_L = mc^2/QB'$. The dimensionless Alfvén speed $\beta'_A = v_A/c = B'/\sqrt{4\pi n_p m_p c^2}$, so that if $B'^2 \propto L_\gamma$, then the equilibrium Lorentz factor γ'_p increases with L unless turbulence with greater total energy is injected at

⁹ There is no difficulty in making strong TeV radiation with an equipartition model; see Fig. 4. Strong flaring VHE or TeV emission in an FSRQ would therefore need to be accompanied by a synchrotron radiation component peaking at X-ray energies, as in the Mrk 501 flare (Pian et al. 1998).

larger size scales (e.g., Sedov radius $\propto \mathcal{E}_{exp}^{1/3}$).

6.8. Spectral Issues

In the models for 3C 279, synchrotron self-absorption invariably sets in at $\sim 10^{12}$ Hz. Even at the sub-mas scale, some slowly varying optically thin radiation must be made as the jet plasma expands and radiates. Our one-zone model omits the complex radio-emitting geometry composed of a superposition of self-absorbed zones and shock-in-jets (cf., Marscher & Gear 1985). A clearer picture of the transition between self-absorbed and optically thin jet plasma can be made with upcoming observations of 3C 279 using the Sub-Millimeter Array (SMA), which operates at 230, 345, and 420 GHz. A regular monitoring would indicate how variability properties differ between these three wavebands, and would make a joint CARMA/OVRO/SMA analysis possible. Radio variability properties can be further compared with data from 15 GHz VLBI MOJAVE monitoring (Lister et al. 2009).

At X-ray energies, the search for inverted spectra at X-ray frequencies, possibly due to the transition from dominant SSC to EC fluxes with increasing photon energy, should be a high priority. The spectral hardening should appear not only in 3C 279, but in most bright FSRQs,¹⁰ and is required from a comparison of Swift and Fermi blazar spectra. The quality of the X-ray data already challenges the model fits, as can be seen from the insets in Figs. 5 and 6. As can also be seen from the insets, the inverted spectrum sets in between about 10 and 40 keV in the 3C 279 SEDs, which is within the Swift XRT range and at the lower end of the BAT energy range. Measurement of X-ray polarization will also help discriminate between SSC and EC processes (Krawczynski 2012).

As to what new information NuStar brings, note that it is much more sensitive in the 6 – 80 keV range than Suzaku, and it is in this range where we predict a hardening from the EC-IR component taking over from the SSC component. Noting already the quality of the X-ray data, high-quality 3C 279 spectra from NuStar should clearly show details of spectral emission components at hard X-ray energies (Harrison et al. 2010). In this regard, it is important that the limitations of the fit at X-ray energies seen in the details of Figs. 5 and 6 can be mitigated if there is an emission component from the hot inner disk near the black hole that shines at hard X-ray energies, like the Shakura-Sunyaev disk can shine through at optical/UV frequencies.

At hard X-ray/ γ -ray energies, the CGRO analysis by McNaron-Brown et al. (1995) showed that the γ -ray peaks are broad, and that the νF_ν peaks of these sources are at $\gg 1$ MeV energies, given the hard spectra for the FSRQs 3C 273, 3C 279, CTA 102, PKS 0528+134, and 3C 45.3 at OSSE (~ 50 keV – 1 MeV) energies. Within the context of this model, the Compton-scattered dust component is essential to explain flux at OSSE levels, which should also be detectable with INTEGRAL, and so would strengthen the case for photons of an IR radiation field being Compton-scattered by jet electrons to γ -ray energies.

Though we have explored a particular paradigm, it remains to be confirmed that the γ -ray emission from the

hard X-ray to $\gg 10$ MeV is scattered IR radiation. Scattered accretion-disk radiation gives a similar emission component (Hartman et al. 2001; Dermer & Schlickeiser 2002), but is further complicated by the precise location of the emitter from the accretion disk. Collisions at various distances from the black hole change dramatically the relative importance of the accretion-disk component.

One thing that is not fully understood is why there is such a large range, by a factor of ≈ 10 for the warm-dust solutions, in energy densities u_{IR} for the IR field implied by the fits. This can be explained if the emission site is on the outer edge of the IR radiation field, where the scattering efficiency rapidly decays. The greatest IR energy density is recorded in Epoch A, implying an IR core of radius ≈ 0.2 pc. This is not so different from our estimates for the BLR radius, $r_{BLR} \sim 0.1$ pc, and for the collision radius $r_{coll} \approx 0.2$ pc. If the size of the IR region inferred from IR luminosity and model energy density to be ~ 0.2 pc, then collisions outside this radius can result in a large reduction of received flux, which could account for the wide range of IR energy densities in Table 4.

6.9. $\gamma\gamma$ opacity constraints

Blazar observables give, within the confines of the one-zone approach, a minimum bulk Lorentz factor Γ from the constraint $\gamma\gamma \rightarrow e^\pm$. If sources are opaque to γ ray escape, then pair re-injection can make a synchrotron or Compton feature, and can initiate further cascade generations. With all its apparent might in the record flare of November 2010, 3C 454.3 was transparent to its own radiation with a bulk Lorentz factor $\Gamma \gtrsim 14$ (Abdo et al. 2011a). This shows, however, that solutions with $\Gamma, \delta_D \lesssim 10 - 15$ also need to include a check on the level of their internal opacity.

The large, $\Gamma \gtrsim 20$ bulk Lorentz factors found in the equipartition model for 3C 279 are consistent with it being transparent to GeV γ rays, so that opacity and cascade emission can be neglected. On the other hand, hadronic secondary γ radiations can be severely absorbed by the IR dust field (Dermer et al. 2012). A further check on the model is to make sure that γ rays can escape the emission region by avoiding internal $\gamma\gamma$ absorption with the synchrotron radiation, and external $\gamma\gamma$ absorption with the Ly α and BLR radiation.

7. SUMMARY

A minimalist prescription drove us to a few-parameter blazar model with which to fit blazar spectra, giving δ_D , B' , and external radiation field energy densities u_{IR} and $u_{Ly\alpha}$ for the IR torus and the BLR field, respectively, as outputs of the fitting procedure. Even in this approach, the simple blazar model has 10 parameters: (1) δ_D , (2) Γ , (3) B' , (4) \mathcal{E}'_e , (5) γ'_p , (6) ϵ_{BLR} , (7) u_{BLR} , (8) ϵ_{IR} , (9) u_{IR} , and (10) b , which is simplified to 6 parameters by assuming $\theta = 1/\Gamma$, $b = 1$, $\epsilon_{BLR} = \epsilon_{Ly\alpha} = 2 \times 10^{-5}$, and ϵ_{IR} corresponds to either 440 K dust (warm dust, $\epsilon_{IR} = 2 \times 10^{-7}$) or 1200 K dust (hot dust, $\epsilon_{IR} = 5.4 \times 10^{-7}$). The six parameters are determined by the observables (1) ν_s , (2) νL_{ν_s} , (3) t_{var} , (4) ν_{SSC} , (5) $\nu L_{\nu_{SSC}}$, (6) ν_C , and (7) νL_{ν_C} ; values for parameters (4) – (7) depend on modeling the overlapping components in the X-ray and γ -ray spectra. An optimum model implies energy densities of the target radiation fields.

¹⁰ Swift BAT spectra of 3C 454.3 and 3C 273 show apparent hardenings above 200 MeV (Ajello et al. 2012).

From fits to 4 epochs of 3C 279, taking $\theta = 1/\Gamma$, $t_{var} = 10^4$ s, and $\zeta_e = 1$, we derive Ly α radiation-field energy densities $u_{Ly\alpha} \sim 0.001 - 0.01$ erg cm $^{-3}$. This is below values expected within the BLR, ~ 0.01 erg cm $^{-3}$, implying that the γ -ray production zone is instead outside the BLR radius $R_{BLR} \sim 0.1 - 0.2$ pc. The wide range of inferred IR energy densities, differing by more than an order of magnitude over the different epochs in the warm-dust solutions, is difficult to explain if the IR radiation field has to vary by such a large factor over the < 7 month period considered here. It therefore seems more likely that the emission regions occur outside the BLR, at $R \sim 0.1 - 0.5$ pc, consistent with relativistic shell collision radii. Gradients in the IR fields in the region containing the BLR in 3C 279 are likewise on the scale of the BLR.

This gives a picture of a system with large IR gradients at the sub-pc scale, comparable to the size scale of the BLR. This might be accomplished most effectively if the molecular torus and accretion disk were part of the same gaseous flow toward the central nucleus.

Within the constraints of the equipartition model presented here (assuming that $t_4 = \zeta_e = 1$), warm-dust solutions were found for all four Epochs A – D, but were only marginally consistent with the blackbody constraint implied by T_{min} in Table 3 in Epochs A and B. Hot-dust solutions were found for Epochs A and B, made possible by the lack of MeV constraints in Epoch A and synchrotron constraints in Epoch B. In Epochs C and D, only warm-dust solutions were possible, and hot-dust solutions were excluded because the target photon frequency was too

large to make any useful spectral contribution at hard X-ray energies.

Concerning the main point of this study, namely the location of the γ -ray emission site in 3C 279, the equipartition model makes a rather definite reply for the Epochs studied. Provided that one accepts the premise of the equipartition model, that the $\zeta_e = 1$ solution is preferred energetically, and assuming $t_{var} = 10^4$ s (which can be improved), then except for Epoch A, where the emission could have taken place inside the BLR, the low Ly α density implies a location outside the BLR, in the range $\sim 0.1 - 0.5$ pc from the central supermassive black hole.

We also find that for powerful blazars like 3C 279, protons satisfy the necessary but not sufficient Hillas condition for acceleration above 10^{20} eV. Though FSRQs are not likely to explain the origin of all UHECRs, UHECRs in FSRQs can make a VHE γ -ray emission component such as has been detected in sources like 3C 279, PKS 1222+216, and possibly PKS 1510-089. Such a feature would be difficult to explain in the framework of the leptonic equipartition model presented here, but the uncertainty related to the variability timescale and equipartition relation makes it hard to draw definite conclusions.

We thank Dr. M. Hayashida for providing the 3C 279 data, and J. D. Finke and S. Razzaque for discussions. The work of C.D.D. is supported by the Office of Naval Research and the NASA *Fermi* Guest Investigator Program.

REFERENCES

- Abdo, A. A., et al. 2009, *ApJ*, 699, 817
—, 2010a, *Nature*, 463, 919
—, 2010b, *ApJ*, 710, 1271
—, 2010c, *ApJ*, 715, 429
—, 2011a, *ApJ*, 733, L26
—, 2011b, *ApJ*, 736, 131
—, 2011c, *ApJ*, 727, 129
—, 2011d, *ApJ*, 726, 43
Ackermann, M., et al. 2010, *ApJ*, 721, 1383
Aharonian, F., et al. 2007, *ApJ*, 664, L71
Ajello, M., Shaw, M. S., Romani, R. W., et al. 2012, *ApJ*, 751, 108
Aleksić, J., et al. 2011, *ApJ*, 730, L8
Arbeiter, C., Pohl, M., & Schlickeiser, R. 2002, *A&A*, 386, 415
Atoyan, A. M., & Dermer, C. D. 2003, *ApJ*, 586, 79
Becker, P. A., Le, T., & Dermer, C. D. 2006, *ApJ*, 647, 539
Błażejowski, M., Sikora, M., Moderski, R., & Madejski, G. M. 2000, *ApJ*, 545, 107
Boettcher, M., Harris, D. E., & Krawczynski, H. 2012, *Relativistic Jets from Active Galactic Nuclei*
Bonnoli, G., Ghisellini, G., Foschini, L., Tavecchio, F., & Ghirlanda, G. 2011, *MNRAS*, 410, 368
Böttcher, M. 2007, *Ap&SS*, 309, 95
Böttcher, M., Reimer, A., & Marscher, A. P. 2009, *ApJ*, 703, 1168
Böttcher, M., & Dermer, C. D. 2002, *ApJ*, 564, 86
Böttcher, M., & Chiang, J. 2002, *ApJ*, 581, 127
Celotti, A., & Fabian, A. C. 1993, *MNRAS*, 264, 228
Celotti, A., & Ghisellini, G. 2008, *MNRAS*, 385, 283
Cerruti, M., Dermer, C.D., Lott, B., Boisson, C., Zech, A., 2013, *ApJL*, submitted
Cholis, I., & Hooper, D. 2012, *arXiv:1211.1974*
Cortina, J. 2012, *The Astronomer's Telegram*, 3965, 1
Dermer, C. D., Schlickeiser, R., & Mastichiadis, A. 1992, *A&A*, 256, L27
Dermer, C. D., & Schlickeiser, R. 1993, *ApJ*, 416, 458
Dermer, C. D. 1995, *ApJ*, 446, L63
Dermer, C. D., Finke, J. D., Krug, H., & Böttcher, M. 2009, *ApJ*, 692, 32; (e) 2012, *ApJ*, 747, 83
Dermer, C. D., & Menon, G. 2009, *High Energy Radiation from Black Holes* (Princeton)
Dermer, C. D., & Razzaque, S. 2010, *ApJ*, 724, 1366
Dermer, C. D., Murase, K., & Takami, H. 2012, *ApJ*, 755, 147
Dermer, C. D., & Schlickeiser, R. 2002, *ApJ*, 575, 667
Dermer, C. D., Miller, J. A., & Li, H. 1996, *ApJ*, 456, 106
Essey, W., & Kusenko, A. 2010, *Astroparticle Physics*, 33, 81
Essey, W., Kalashev, O. E., Kusenko, A., & Beacom, J. F. 2010, *Physical Review Letters*, 104, 141102
Finke, J. D., Dermer, C. D., & Böttcher, M. 2008, *ApJ*, 686, 181
Finke, J. 2012, *ApJ*, in press, *arXiv:1212.0869*
Foschini, L., Ghisellini, G., Tavecchio, F., Bonnoli, G., & Stamerra, A. 2011, *A&A*, 530, A77+
Fossati, G., Maraschi, L., Celotti, A., Comastri, A., & Ghisellini, G. 1998, *MNRAS*, 299, 433
Georganopoulos, M., Kirk, J. G., & Mastichiadis, A. 2001, *ApJ*, 561, 111
Ghisellini, G., Maraschi, L., & Tavecchio, F. 2009, *MNRAS*, 396, L105
Ghisellini, G., Celotti, A., Fossati, G., Maraschi, L., & Comastri, A. 1998, *MNRAS*, 301, 451
Ghisellini, G., & Tavecchio, F. 2008, *MNRAS*, 387, 1669
Giannios, D., Uzdensky, D. A., & Begelman, M. C. 2009, *MNRAS*, 395, L29
Gu, M., Cao, X., & Jiang, D. R. 2001, *MNRAS*, 327, 1111
Harrison, F. A., Boggs, S., Christensen, F., et al. 2010, *Proc. SPIE*, 7732,
Hartman, R. C., et al. 1992, *ApJ*, 385, L1
—, 2001, *ApJ*, 553, 683
Hayashida, M., et al. 2012, *ApJ*, 754, 114
Hillas, A. M. 1984, *ARA&A*, 22, 425
Jones, F. C. 1968, *Physical Review*, 167, 1159
Koratkar, A., Pian, E., Urry, C. M., & Pesce, J. E. 1998, *ApJ*, 492, 173

- Krawczynski, H. 2012, *ApJ*, 744, 30
- Lähteenmäki, A., & Valtaoja, E. 1999, *ApJ*, 521, 493
- Lister, M. L., Aller, H. D., Aller, M. F., et al. 2009, *AJ*, 137, 3718
- MAGIC Collaboration, Albert, J., et al. 2008, *Science*, 320, 1752
- Malmrose, M. P., Marscher, A. P., Jorstad, S. G., Nikutta, R., & Elitzur, M. 2011, *ApJ*, 732, 116
- Marscher, A. P., & Gear, W. K. 1985, *ApJ*, 298, 114
- Marziani, P., Sulentic, J. W., Dultzin-Hacyan, D., Calvani, M., & Moles, M. 1996, *ApJS*, 104, 37
- Massaro, E., Perri, M., Giommi, P., & Nesci, R. 2004, *A&A*, 413, 489
- Massaro, E., Tramacere, A., Perri, M., Giommi, P., & Tosti, G. 2006, *A&A*, 448, 861
- Massaro, F., Grindlay, J. E., & Paggi, A. 2010, *ApJ*, 714, L299
- McNaron-Brown, K., Johnson, W. N., Jung, G. V., et al. 1995, *ApJ*, 451, 575
- Meyer, E. T., Fossati, G., Georganopoulos, M., & Lister, M. L. 2011, *ApJ*, 740, 98
- Moderski, R., Sikora, M., & Błażejowski, M. 2003, *A&A*, 406, 855
- Murase, K., Dermer, C. D., Takami, H., & Migliori, G. 2012, *ApJ*, 749, 63
- Murase, K. 2012, *ApJ*, 745, L16
- Murase, K., & Takami, H. 2009, *ApJ*, 690, L14
- Nenkova, M., Sirocky, M. M., Ivezić, Ž., & Elitzur, M. 2008, *ApJ*, 685, 147
- Nenkova, M., Sirocky, M. M., Nikutta, R., Ivezić, Ž., & Elitzur, M. 2008, *ApJ*, 685, 160; (e) 2010, *ApJ*, 723, 1827
- Park, B. T., & Petrosian, V. 1995, *ApJ*, 446, 699
- Pian, E., Vacanti, G., Tagliaferri, G., et al. 1998, *ApJ*, 492, L17
- Punch, M., et al. 1992, *Nature*, 358, 477
- Sari, R., Piran, T., & Narayan, R. 1998, *ApJ*, 497, L17
- Sikora, M., Begelman, M. C., & Rees, M. J. 1994, *ApJ*, 421, 153
- Sikora, M., Stawarz, L., Moderski, R., Nalewajko, K., & Madejski, G. M. 2009, *ApJ*, 704, 38
- Sokolov, A., & Marscher, A. P. 2005, *ApJ*, 629, 52
- Stoeckle, J. T., Danforth, C. W., & Perlman, E. S. 2011, *ApJ*, 732, 113
- Tanaka, Y. T., et al. 2011, *ApJ*, 733, 19
- Telfer, R. C., Zheng, W., Kriss, G. A., & Davidsen, A. F. 2002, *ApJ*, 565, 773
- Tramacere, A., Massaro, E., & Taylor, A. M. 2011, *ApJ*, 739, 66
- Wagner, S. J., Behera, B., & H.E.S.S. Collaboration. 2010, in *Bulletin of the American Astronomical Society*, Vol. 42, AAS/High Energy Astrophysics Division #11, 660
- Wehrle, A. E., et al. 1998, *ApJ*, 497, 178
- Woo, J.-H., & Urry, C. M. 2002, *ApJ*, 579, 530